Supplementary Information

Reactive tunnel junctions in electrically-driven plasmonic nanorod metamaterials

Pan Wang[,†], Alexey V. Krasavin[†], Mazhar E. Nasir, Wayne Dickson, and Anatoly V. Zayats[*]*

[†]These authors contributed equally to this work

[*]Corresponding author: pan.wang@kcl.ac.uk, a.zayats@kcl.ac.uk

S1. Fabrication of plasmonic nanorod metamaterials

The plasmonic nanorod metamaterials were electrochemically grown in substrate-supported, porous, anodized aluminum oxide (AAO) templates [S1]. The substrate is a multilayered structure comprised of a 1 mm thick glass slide, a 10 nm thick tantalum oxide adhesive layer, and a 7 nm thick Au film acting as a working electrode for the electrochemical reaction. An aluminum film of up to 500 nm thickness is then deposited onto the substrate by planar magnetron sputtering. The aluminum film is subsequently anodized in 0.3 M oxalic acid at 40 V to produce the porous AAO template. The diameter, separation and ordering of the Au rods in the assembly are determined by the geometry of the AAO template and thus, by the anodization conditions. These parameters, in addition to the rod length, can be tuned to control the optical properties of the nanorods throughout the visible and near-infrared spectral regions [S1,S2]. Au electrodeposition is performed with a three-electrode system using a non-cyanide solution. The length of nanorods is controlled by the electrodeposition time. In this work, Au nanorods were overgrown to fully fill the AAO pores until a layer of Au was formed on the top of AAO template and the samples were ion-milled as described in Section S2.

S2. Ion milling of plasmonic nanorod metamaterials

To remove the overgrown Au layer on the surface of AAO template and make the tips of Au nanorods slightly lower than the surrounding Al_2O_3 matrix, as-fabricated plasmonic nanorod metamaterials were ion-milled (V6000 mill & sputter system, Scientific Vacuum Systems). The milling parameters were set as follows: base pressure, 2×10^{-6} mBar; acceleration voltage, 1000 V; beam voltage, 500 V; beam current, 23 mA; rotation speed of the sample holder, 58 RPM. The metamaterials were milled at an oblique angle of 75º with respect to the normal to the sample surface and the milling time was set to be 50 min. Because the milling rate of Al_2O_3 is about one order of magnitude lower than that of Au [S3], the surrounding Al_2O_3 matrix worked as a mask to make the Au nanorod tips slightly lower than the

Al$_2$O$_3$. After ion milling, the nanorod metamaterials were stored in 200 proof ethanol to avoid contamination in air.
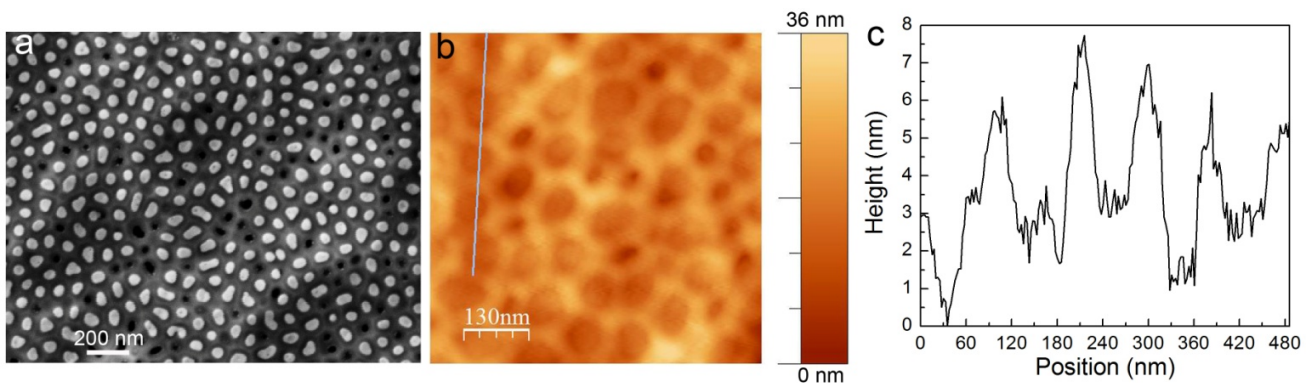

Figure S1 | Surface morphology of the plasmonic nanorod metamaterial shown in Fig. 1c. a, SEM planar view of the nanorod metamaterial after ion milling. **b**, AFM topography of the nanorod metamaterial. **c**, Height contour across the line in (**b**).

Figures S1a and S1b present surface morphology of a plasmonic nanorod metamaterial after ion milling obtained using scanning electron microscopy (SEM) and atomic force microscopy (AFM), respectively. The surface is relatively smooth with dips which correspond to the positions of the Au nanorods, surrounded by the higher Al$_2$O$_3$ barriers. Figure S1c shows the height contour measured across the line drawn in Fig. S1b, it can be clearly seen that the Au nanorod tips are ~4 nm lower than the surrounding Al$_2$O$_3$ matrix, which is ideal for the construction of metal-air-metal tunnel junctions.

The distance between the nanorod tips and the surrounding Al$_2$O$_3$ matrix, which determines the thickness of metal-air-metal tunnel junctions (see details in Section S4), can be controlled by the milling angle. The higher the milling angle used, the smaller the distance between the nanorod tips and the surrounding Al$_2$O$_3$ matrix can be obtained. For the construction of metal-air-metal tunnel junctions, theoretically it is better to have smaller distance which can produce higher tunnelling current, emission intensity and hot-electron generation rate. However, the fabrication yield and the stability of devices decrease significantly with the deceasing gap distance due to the easier short-circuiting of junctions and heat generated under higher tunnelling current. Considering both the fabrication yield and the

performance of the device, we used milling angle of 75º which can produce the best samples in all the experiments.

S3. Fabrication of electrically-driven plasmonic nanorod metamaterials

Figure S2a shows the schematic steps for the fabrication of electrically-driven plasmonic nanorod metamaterials. Firstly, an Au wire was attached to the aluminum film (it's electrically connected to the Au nanorods through the 7 nm thick Au film, see Section S1) using silver conductive paste; secondly, a polydimethylsiloxane (PDMS) slab with an open window in the middle was placed onto the nanorod array region; finally, another PDMS slab with an EGaIn droplet and an Au wire on it was set onto the first PDMS slab, with the EGaIn droplet sitting exactly in the open window and contacting with the nanorod array to form millions of tunnel junctions.
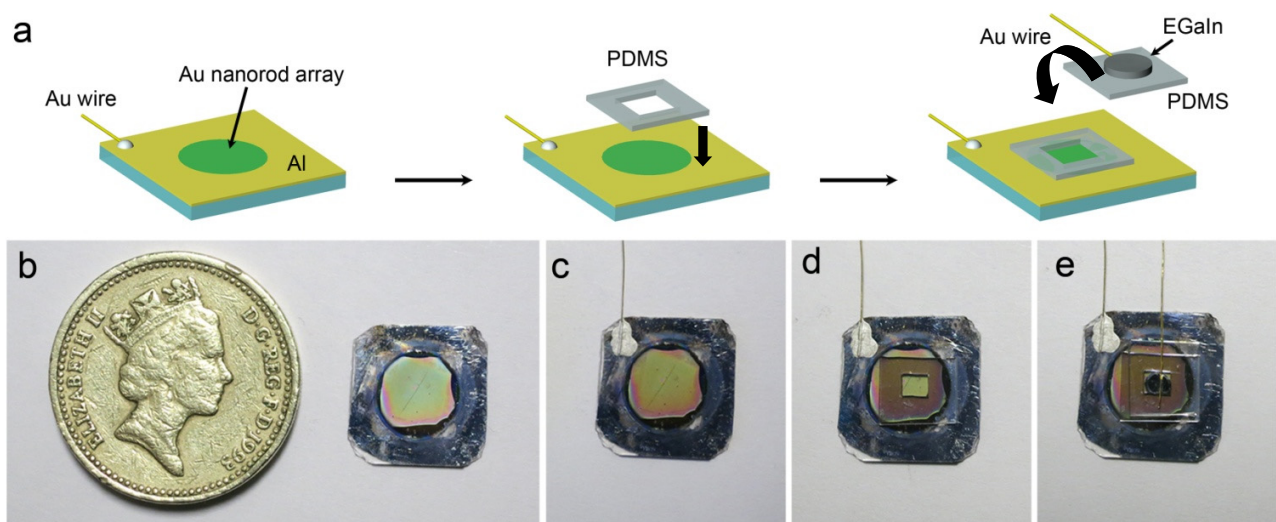

Figure S2 | Steps for the fabrication of electrically-driven plasmonic nanorod metamaterials. a, Schematic diagram of the fabrication steps. **b**, Photograph of a plasmonic nanorod metamaterial together with a one pound coin. **c–e**, Photographs of the corresponding fabrication steps.

Figure S2b shows a photograph of a plasmonic nanorod metamaterial, the size of the substrate is 12 × 12 mm. The Au nanorod array is located in the middle area of the sample and has a greenish colour.

Figure S2c–e present photographs of the metamaterial after each fabrication step, showing the ease of fabrication. The area of the tunnel junctions is determined by the contact area of the EGaIn droplet with the Au nanorod array, which in this case is as large as several mm^2.

S4. Estimation of tunnel junction thickness

Due to the liquid nature of EGaIn, it is difficult to prepare cross-sectional samples for the precise characterization of the metal-air-metal tunnel junction thickness using transmission electron microscopy. However, it can be estimated theoretically via the numerical simulations. The band diagram of the tunnelling junction was determined on the basis of work function, electron affinity and band width data available in the literatures [S4,S5]. For the calculation of the tunnelling current, a non-trivial profile of the barrier was discretized into an ensemble of rectangular sections and the tunnelling current was calculated using the transfer matrix method [S6] (a mistake in the matrix multiplication sequence was found in Ref. [S6] and corrected) implemented in a custom-made MATLAB code. The calculation procedure was benchmarked on the case of a rectangular barrier, allowing an analytical solution, and returned correct results. In the calculation of the tunnelling through the metamaterial structure the thicknesses of the air gap and the Ga$_2$O$_3$ layer were varied and the correct values were found by matching the magnitude and the asymmetry of the calculated current-voltage curve to the experimentally observed one. The thickness of the air gap was found to be ~1.15 nm, and the thickness of the Ga$_2$O$_3$ layer is in agreement with the data reported in the literature [S7].

As shown in Fig. S1, the Au nanorod tips are ~4 nm lower than the surrounding alumina matrix. When a droplet of EGaIn was added onto the metamaterial surface, it was supported by the alumina matrix. This is due to the existence of a thin protective layer of Ga$_2$O$_3$ on the surface [S7] after exposure in air, which can help to maintain the structural stability of the EGaIn droplet and prevent the flow of EGaIn liquid into the template. However, the EGaIn can deform slightly into the pores. In this case, it is reasonable for the EGaIn surface to deform ~3 nm to form air gaps with the nanorod tips with average

thickness of ~1.15 nm. It is worth noting that it is inevitable that some nanorod tips may contact directly with the EGaIn surface to short-circuit the device when the contact area between the EGaIn and the metamaterial is in macroscopic scale. However, the large current flows through the short-circuited rods can melt them quickly, ruling out the shorted nanorods automatically.

S5. Estimation of inelastic tunnelling efficiency

The overall electron-to-photon conversion efficiency $\eta_{el-phot} = \eta_{inel} \cdot \eta_{ant}$ is determined by two factors: 1) efficiency of inelastic electron tunnelling $\eta_{inel} = \Gamma_{inel}/\Gamma_{tot}$ (where Γ_{inel} and Γ_{tot} are inelastic and total tunnelling rates, respectively), and 2) antenna radiative efficiency $\eta_{ant} = P_{rad}/P_{tot}$, defining how much power from the excited plasmonic modes is radiated in light. Estimating the $\eta_{el-phot}$ (~8.1 × 10^{-7}) from the ratio of emitted photons (measured emission power ~100 nW, assuming all the emitted photons have the same wavelength of 850 nm) to injected electrons (tunnelling current ~0.085 A under 2.5 V forward bias for 4 mm^2 surface area) and evaluating η_{ant} (~0.001, the whole nanorod metamaterial works as an antenna in this case) from numerical simulations, the efficiency of the inelastic tunnelling process is found to be around 0.1%, a value which is consistent with previous experimental observations [7]. Interpreting the experimental results here, one needs to keep in mind that the estimated value is an averaged characteristic of an ensemble of nanorods, which have variation in heights and some tip profiles. On the other hand, one should take into account that radiation efficiency of the metamaterial η_{ant} depends on the particular set of the excited plasmonic modes, which in turn depends in principle on the position across the nanorod tip where tunnelling happen. Thus, in the numerical simulations η_{ant} was averaged over the tip area, although it was found that the tunnelling position has only a minor influence. Theoretically, the inelastic tunneling efficiencies were predicted to reach few or even tens of percents [28,29,S8,S9]. The strategies for such increase could be derived from the physical nature of the involved processes. Generally, the efficiency of inelastic tunnelling is defined by both electronic densities of states in the 'source' and 'drain' electrodes (as well as by any electronic

states inside the junction region－electronic LDOS), as well as local density of electromagnetic states in the tunnel junction－optical LDOS. Thus, the first strategy is related to engineering the electronic LDOS by introducing quantum well-based tunnelling structures [S8,S9] or introducing molecules or atoms in the tunnelling gap [S10]. The second strategy is connected with the design of electromagnetic properties on the system, which also can be used to enhance the radiation efficiency η_{ant} [6–8]. The latter, and particularly its spectral dependence, can be easily engineered by the metamaterial design [S2].

S6. Optical characterization setup

As shown in Fig. S3a, the electrically-driven plasmonic nanorod metamaterial was mounted vertically on a sample holder, which was then connected to a power supply for the electric excitation and an ammeter to monitor the tunnelling current. A 20X objective was used to collect the light emission from the substrate side of the metamaterial, which was then redirected to a spectrometer equipped with a charge-coupled device (CCD) for spectral analysis. All the obtained emission spectra were normalized using the spectral response function of the apparatus shown in Fig. S3b.
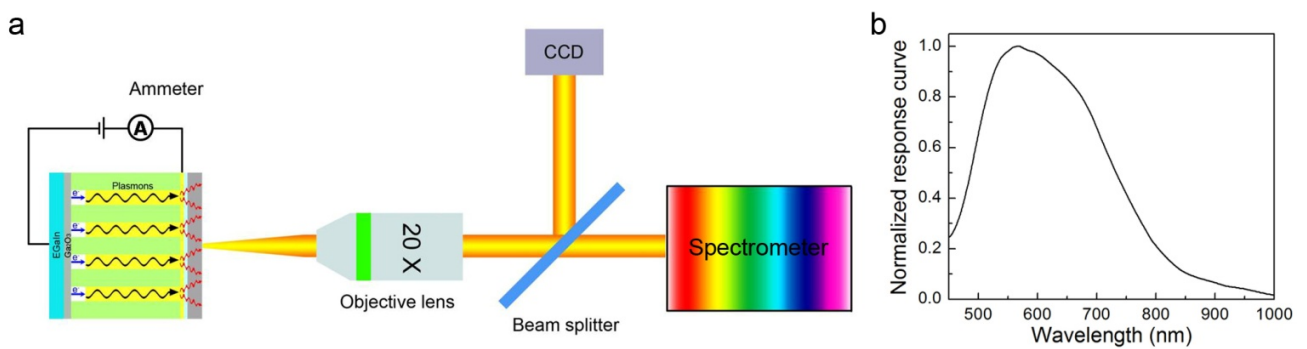

Figure S3 | Optical characterization of electrically-driven plasmonic nanorod metamaterials. a, Schematic diagram of the optical characterization setup. **b**, Normalized spectral response of the detection system, which includes the transmission through the objective lens, beam splitter, optical fibre, reflectivity of grating in the spectrometer, and the quantum efficiency of the CCD in the spectrometer.

S7. The relation between emission power and tunnelling current

As shown in Fig. S4, the emission power of the electrically-driven plasmonic nanorod metamaterial increases linearly with the increasing tunnelling current.
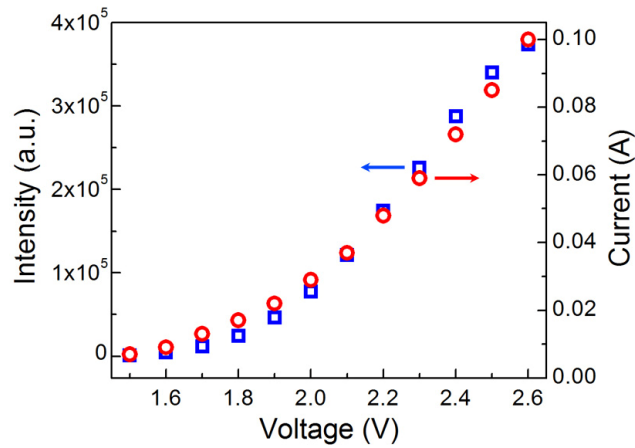

Figure S4 | The dependence of emission power and tunnelling current on the applied bias. The dependence of the integrated emission power obtained from the spectra in Fig. 2d (blue hollow squares) and the measured tunnelling current (red hollow circles) on the applied forward bias.
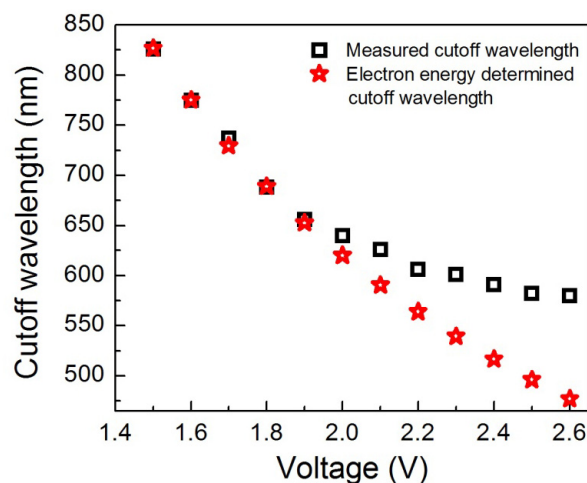
S8. Bias-dependent cutoff wavelength

Figure S5 | Bias-dependent cutoff wavelength. The dependence of the cutoff wavelength of the spectra in Fig. 2d (black hollow squares) on the applied forward bias. The theoretical cutoff wavelength is defined by $hc/\lambda_{cutoff} = |eV_b|$ (red hollow stars).

For the emission generated by inelastically tunnelled electrons, the energy of the emitted photons is always less than the energy of tunnelling electrons [1] and have a high-frequency cutoff λ_{cutoff} defined by the relation $h\nu_{cutoff} = hc/\lambda_{cutoff} = |eV_b|$, where ν_{cutoff} is the high-frequency cutoff, and V_b is the applied bias. As shown in Fig. 2d and Fig. S5, this behavior is indeed observed confirming the excitation mechanism.

S9. Stability of electrically-driven nanorod metamaterials

Figure S6a shows the light emission stability of an electrically-driven nanorod metamaterial (measured in Fig. 2) when the forward bias was switched between 0 and 2.5 V. The light emission intensity remained at almost the same level after each on-off cycle, indicating a good on-off stability of the device. Figure S6b shows recorded emission spectra (every 0.5 h) of the electrically-driven plasmonic nanorod metamaterial during a 2-h experimental period when a constant forward bias of 2.6 V was applied. The intensity and shape of the emission spectra were virtually unchanged, indicating a long-term operation stability of the device, which is of vital importance for practical applications.
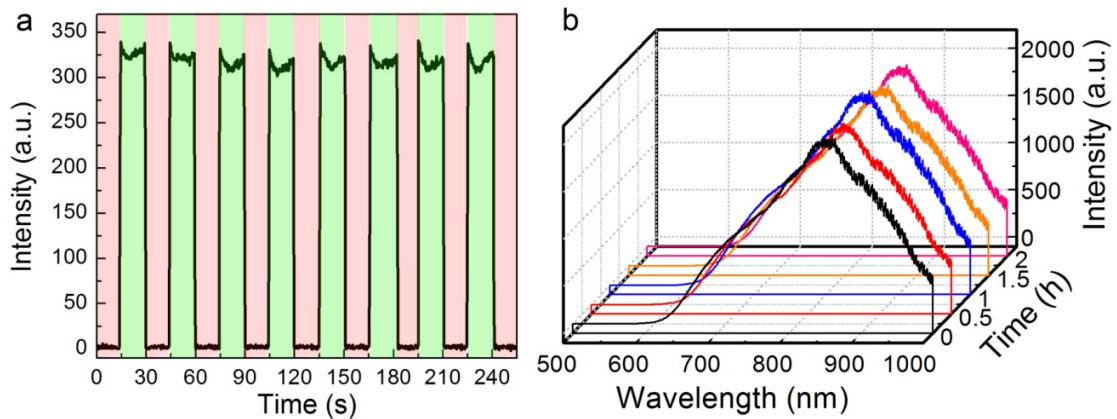

Figure S6 | Emission stability of the electrically-driven plasmonic nanorod metamaterial. a, On-off stability of the device when the forward bias was switched between 0 (red-colored area) and 2.5 V (green-colored area). **b**, Long-term emission stability of the continuously operated device under 2.6 V forward bias.

S10. Controlled etching of Al$_2$O$_3$ matrix

A wet chemical etching method was used to controllably remove the Al$_2$O$_3$ matrix surrounding the Au nanorods in the plasmonic nanorod metamaterials. Briefly, the ion-milled nanorod metamaterial stored in 200 proof ethanol was firstly dried under N$_2$ and then put into an aqueous solution of 3.5% H$_3$PO$_4$ at 35 ℃ to start the etching. The etching depth can be precisely controlled by the etching time, as shown in Fig. S7. We used 10 min to remove ~20 nm surrounding Al$_2$O$_3$ matrix for the sample shown in Fig. 3b. After the chemical etching, the metamaterial was washed several times in 18.2 MΩ deionized water (DI water) to remove chemicals on the surface and then kept in DI water for future use.
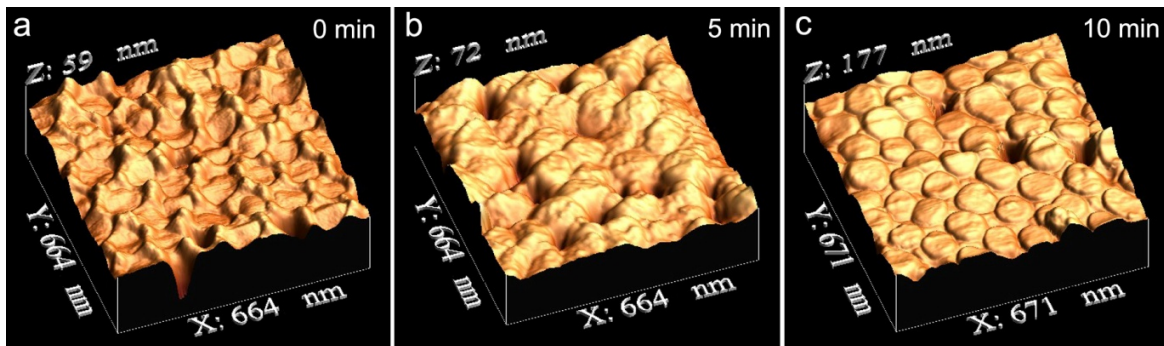

Figure S7 | Surface topography of a plasmonic nanorod metamaterial measured during the etching process. a, Before etching. **b**, After 5-min etching. **c**, After 10-min etching.

S11. Self-assembly of polymer monolayer on exposed Au nanorods

A self-assembly approach was used to functionalize the exposed Au nanorods with a monolayer of polymer; in particular poly-L-histidine (PLH, M$_w$ 5,000-25,000, Sigma-Aldrich) was used in this work. Firstly, ~5 mg PLH powder was dissolved into 5 mL DI water and the pH of the solution was adjusted to 5–6 using 0.1 N HCl. Secondly, the etched plasmonic nanorod metamaterial was submerged into the PLH solution and incubated for 0.5 h. Due to the high affinity of imidazole and amino groups of PLH to Au and the positive charging of protonated PLH in solution, a monolayer of PLH self-assembled on the exposed Au nanorod surface (the thickness of the monolayer was determined to be ~1.7 nm by using

transmission electron microscopy of PLH coated Au nanorods). Finally, the metamaterial was washed several times in DI water to remove weakly bound PLH and dried under N_2 for the further development of metal-PLH-metal tunnel junctions.

The PLH layer has two roles. Firstly, it works as a nanometer-scale spacer to separate the EGaIn droplet and the Au nanorod tips (to prevent direct contact and short-circuiting the device), thus, it is the tunnel barrier. Secondly, PLH is a reactant, it is chosen to demonstrate the reactive property of the tunnel junctions, because the NH group in the imidazole rings and/or amino groups of PLH near the nanorod tips can undergo oxidative dehydrogenation and coupling reactions with the help of hot electrons and oxygen, similar to the oxidative formation of azo species from aniline group molecules in the presences of hot electrons and oxygen [31,34–36].

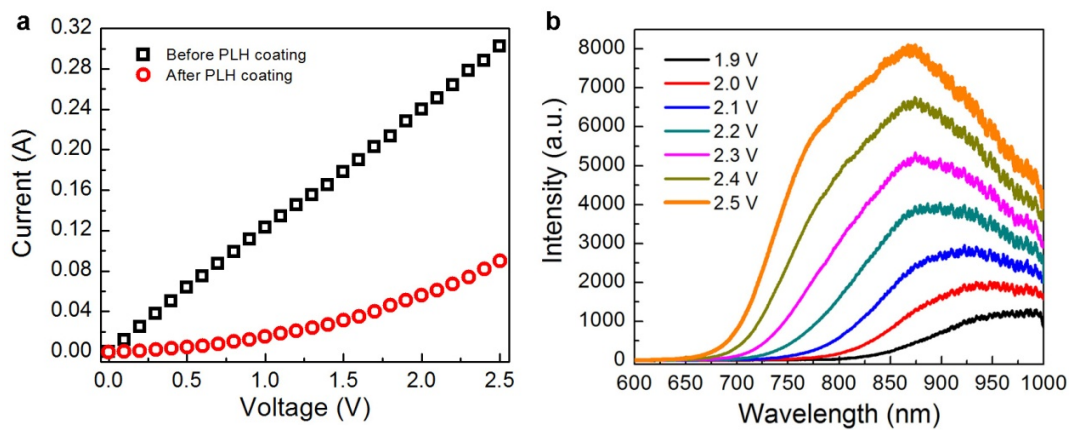# S12. Characterization of the metal-PLH-metal tunnel junctions

Figure S8 | Metal-polymer-metal tunnel junctions. a, current-voltage curves for an etched metamaterial measured before (black hollow squares) and after (red hollow circles) the self assembly of PLH monolayer. Note that the contact areas for the two measurements are different. **b**, Measured emission spectra of the electrically-driven PLH-functionalized metamaterial for different applied forward biases.

Figure S8a shows current-voltage curves of the etched plasmonic nanorod metamaterial measured before and after the self-assembly of PLH monolayer. Compared to the linear response of current-voltage curve of the freshly etched metamaterial measured using EGaIn (black hollow squares), the current-voltage curve is nonlinear after the coating of a monolayer of PLH (red hollow circles), indicating the tunnelling of electrons through the tunnel barrier between the Au nanorod tips and the EGaIn (PLH monolayer in this case). This is also verified by the observation of light emission from the device when a 2.5 V forward bias was applied. The dependence of the emission spectrum for the metal-PLH-metal tunnel junctions on the applied bias is presented in Fig. S8b.

S13. Gas-cell for the investigation of reactive tunnel junctions

The experiment for the investigation of reactive tunnel junctions was carried out by placing an electrically-driven plasmonic nanorod metamaterial in a sealed 10-mL gas cell (Fig. S9). For the quick diffusion of analyte gas into the tunnel junctions, as shown in Fig. S9a, one side of the bottom PDMS slab was removed. A constant forward bias of 2.5 V was applied to the nanorod metamaterial and an ammeter was used to monitor the tunnelling current. The analyte gases (N_2, 2% H_2 in N_2, O_2, and 2% H_2 in N_2 with 75% RH) were introduced into the gas cell through a gas inlet at a flow rate of about 50 cm^3/min. Ambient air with a RH of 26% was introduced into the cell through the gas outlet by diffusion while the gas inlet was closed. The light emission from the substrate side of the electrically-driven plasmonic nanorod metamaterial was recorded every 50 s to optically probe the states of the tunnel junctions. All experiments were carried out at room temperature and under atmospheric pressure.
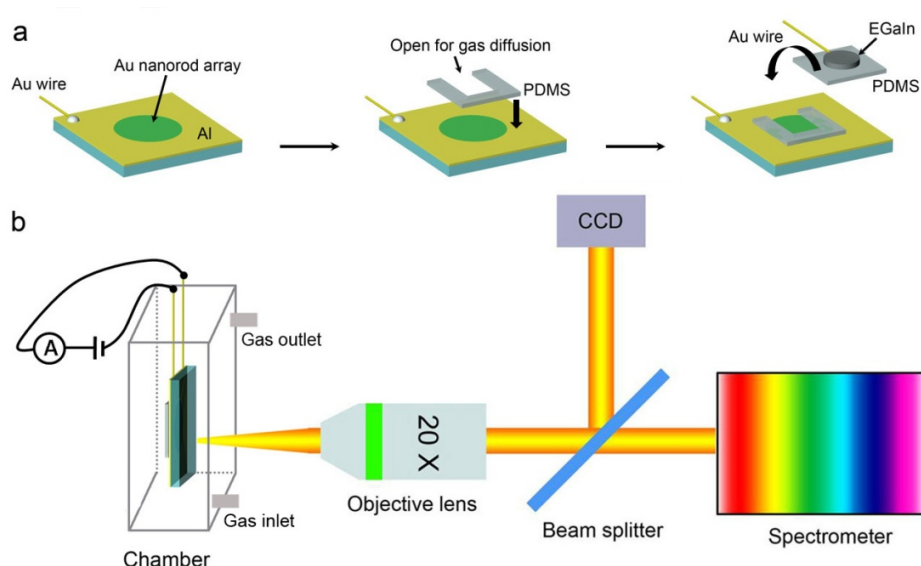
Figure S9 | Setup for the investigation of reactive tunnel junctions. a, Schematic diagram of the fabrication steps of the electrically-driven plasmonic device for the investigation of reactive tunnel junctions. **b**, Schematic diagram of the experimental setup.

S14. Response of the reactive tunnel junctions to different gases

We have tested the response of electrically-driven plasmonic nanorod metamaterial under different atmospheres including air with 26% RH, N_2, 2% H_2 in N_2, O_2 (made by decomposition of hydrogen peroxide), and 2% H_2 in N_2 with 75% RH. The emission spectra were recorded every 50 s. Figure 3e shows the dynamic change of integrated emission power during the test. At the beginning, the device was operated in air until a stable light emission was reached. When the cell atmosphere was switched between air and N_2 (0-750 s), the emission intensity stayed at almost the same level, which means that the emission change in Fig. 3d is caused by the reaction of tunnel junctions with H_2 molecules. When the cell atmosphere was switched between air and 2% H_2 in N_2 (750-1950 s), excellent reversibility and reproducibility of the changes in the light emission was observed. When the atmosphere was switched between air, O_2 and 2% H_2 in N_2 (2800-3900 s), the tunneling/emission changes are the same as in measurements between 750 and 1950 s, indicating that O_2 in air is responsible for the emission changes in Fig. 3c. Finally, measurements between 3900-4850 s further indicate that the change in relative

humidity has a negligible effect on the reactions. Based on the above analysis, it can be confirmed that the observed emission changes in Fig. 3c is caused by the reaction of tunnel junctions with O_2 molecules in air and the observed emission changes in Fig. 3d is caused by the subsequent reaction of tunnel junctions with H_2 molecules.

As shown in Figs. 3c-3e, the emission intensity increases (or decreases) gradually with the introduction of air (or 2% H_2 in N_2), and then reaches saturation. Despite of the difficulty in the direct measurement of the chemical reaction efficiency, the time-dependent emission changes can reflect the progress of the reactions taking place in the junctions. The gradual change of emission intensity indicates that the reaction is in progress, and the saturation indicates the completeness of the reactions in all the tunnel junctions. From Figs. 3c-3e, we can learn that it takes several minutes to complete the oxidation or reduction reactions. This is due to on the one hand the highly confined nature of metal-PLH-metal tunnel junctions which hinders the fast diffusion of gas molecules, and on the other hand the high-density and extremely large number of tunnel junctions which prolong the response time of the whole system. This can be improved by further optimizing the structure and/or decreasing the tunnel junction areas.

S15. Dependence of chemical reactions on applied bias and external light illumination

First, the dependence of chemical reactions on the applied bias voltage was tested. Figure S10 shows the sequence of integrated emission power measurements when test biases of 2.5, 2.0, 1.5, 1.0, 0.5, and 0 V were applied to the device. Data presented in Fig. S10a-f were measured when the cell atmosphere was switched from ambient air to 2% H_2 in N_2 and the data presented in Fig. S10g-l were measured when the cell atmosphere was switched from 2% H_2 in N_2 to air. When the cell atmosphere was switched from air to 2% H_2 in N_2 (Fig. S10a-f), the emission intensity decreased 100% to the lowest value (from the second black circle to the first red circle, Fig. S10a) when a test bias of 2.5 V was applied to the device

for 10 min; the emission intensity decreased ~66% (Fig. S10b), ~36% (Fig. S10c), ~13% (Fig. S10d), ~12% (Fig. S10e), and ~2% (Fig. S10f) when a test bias of 2.0, 1.5, 1.0, 0.5, and 0 V was applied for 10 min, respectively. When the cell atmosphere was switched from 2% H_2 in N_2 to air (Fig. S10g-l), the emission intensity increased 100% to the highest value (Fig. S10g) when a test bias of 2.5 V was applied to the device for 10 min; the emission power increased ~57% (Fig. S10h), ~30% (Fig. S10i), ~26% (Fig. S10j), ~20% (Fig. S10k), and ~19% (Fig. S10l) when a test bias of 2.0, 1.5, 1.0, 0.5, and 0 V was applied for 10 min, respectively. The above results indicate that the chemical reactions involving O_2 and H_2 molecules in the tunnel junctions are highly dependent on the applied bias, the higher the applied bias (higher hot-electron energy and generation rate), the quicker the emission intensity changes (also see Fig. 4a).
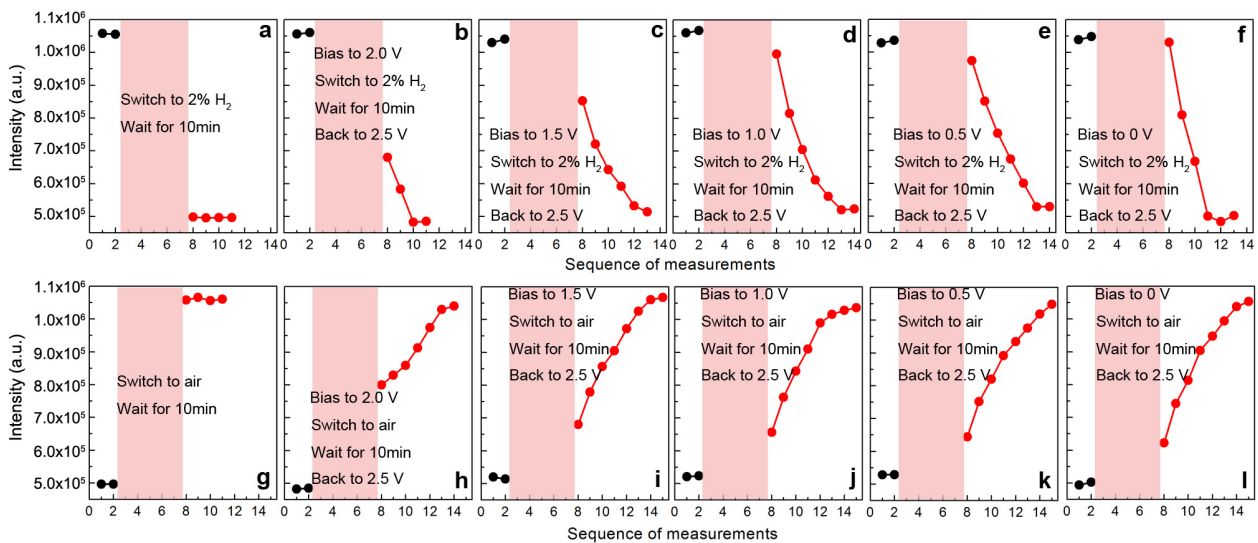

Figure S10 | Dependence of chemical reactions on applied bias. a-f, Dependence of the chemical reaction in the tunnel junctions on the test bias of 2.5 (**a**), 2.0 (**b**), 1.5 (**c**), 1.0 (**d**), 0.5 (**e**), and 0 V (**f**) when the cell atmosphere was switched from air to 2% H_2 in N_2 revealed by changes in the emission intensity. **g-l,** Dependence of the chemical reaction in the tunnel junctions on the test bias of 2.5 (**g**), 2.0 (**h**), 1.5 (**i**), 1.0 (**j**), 0.5 (**k**), and 0 V (**l**) when the cell atmosphere was switched from 2% H_2 in N_2 to air revealed by changes in the emission intensity.

In order to further confirm the role of hot electrons in the reactions of tunnel junctions with O_2 and H_2 molecules, we tested the effect of external light illumination on the reactions in the unbiased tunnel junctions. In these experiments, the metamaterial was illuminated in the chosen spectral range from the substrate side using a colour-filtered broadband halogen light source providing a power density of ~0.1 W cm^{-2}. Initially, the device was stabilized in an atmosphere of either ambient air or 2% H_2 in N_2 under the sensing bias of 2.5 V to record the emission spectrum characteristic of the tunnel junctions. After the reference spectrum was recorded, the bias was removed (V_b = 0 V), the cell atmosphere was immediately switched, and the device was illuminated by the light in a chosen spectral range for 10 min. In order to monitor the chemical reactions taken place during the illumination, after the external illumination was switched off, the emission spectrum from the device was recorded under a sensing bias of 2.5 V. The sensing bias was kept on and the emission spectra were recorded every 50 s until the device reached saturation and was ready for the next cycle. Figure S11 shows the sequence of the measurements for different atmospheres and external illumination spectra. Please note that for the chemical reaction in the tunnel junctions involving O_2 molecules (observed when the cell atmosphere switched from 2% H_2 in N_2 to air, Fig. S11a-d), the signal increased by ~21% (from the second black circle to the first red circle, Fig. S11a) without external illumination and bias (the same as shown in Fig. S10l) due to the reaction taking place during 50 s of the measurement under the sensing bias. However, when the unbiased tunnel junctions were illuminated by light with wavelength larger than 500 nm for 10 min, the signal increased 100% to the highest value (Fig. S11b). The illumination in the spectral range of 500-750 nm (power density of ~0.024 W cm^{-2}) gives a similar result (Fig. S11c). However, the illumination by light with wavelength larger than 800 nm (power density of ~0.062 W cm^{-2}) has no appreciable influence on the reaction (Fig. S11d). It can be noted that in the wavelength range of 500-750 nm, the surface plasmons can be efficiently excited related to the nanorods forming the metamaterial (inset of Fig. 4b), while at the longer wavelength (> 800 nm), the excitation efficiency is low. This suggests that the chemical reaction in the unbiased tunnel junctions involving O_2 under

external illumination was mediated by the hot electrons (generated via the non-radiative decay of plasmons), confirming the important role of tunnelling-generated hot electrons in the reactive tunnel junctions.
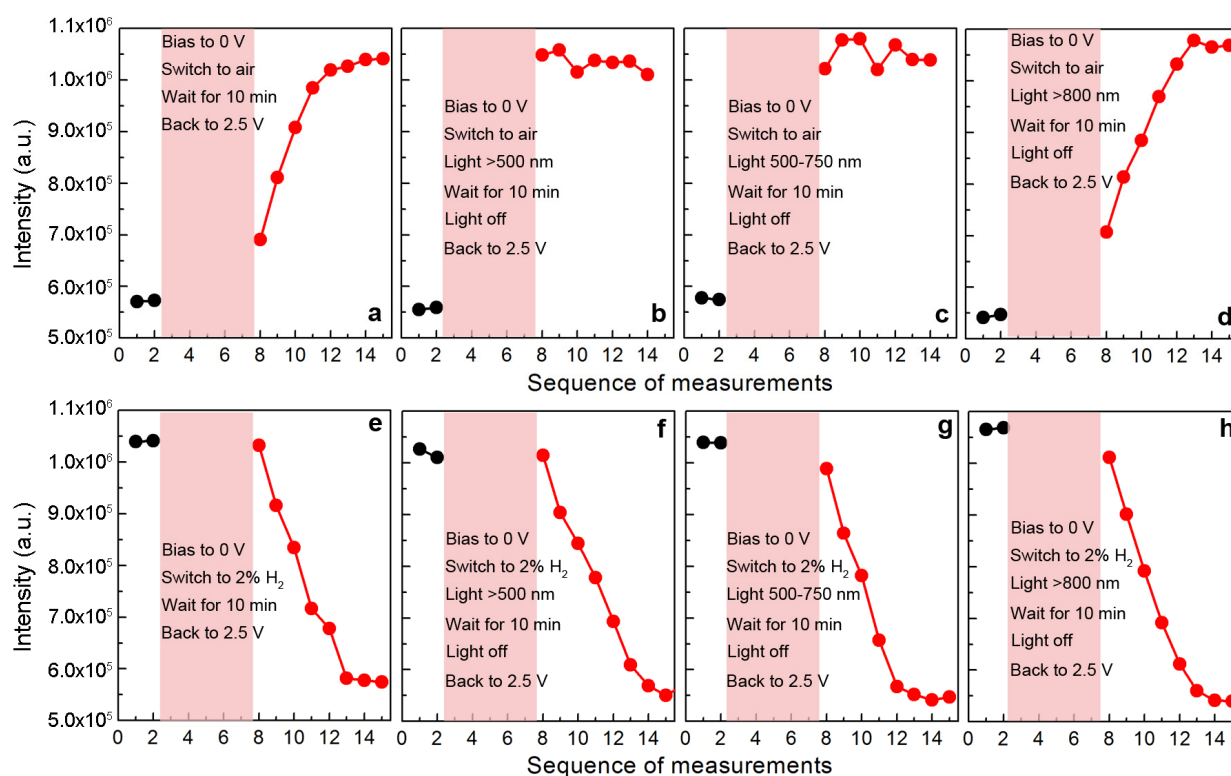

Figure S11 | Dependence of chemical reactions on external light illumination. a-d, Dependence of chemical reaction in the tunnel junctions on external illumination when the cell atmosphere was switched from 2% H_2 in N_2 to air revealed by changes in the emission intensity. The unbiased device was kept in darkness (**a**) or illuminated by light with wavelength of >500 nm (**b**), 500-750 nm (**c**), and >800 nm (**d**) during the 10-min test period (pink-shaded area). **e-h,** Dependence of chemical reaction in the tunnel junctions on external illumination when the cell atmosphere was switched from air to 2% H_2 in N_2 revealed by changes in the emission intensity. The unbiased device was kept in darkness (**e**) or illuminated by light with wavelength of >500 nm (**f**), 500-750 nm (**g**), and >800 nm (**h**) during the 10-min test period (pink-shaded area).

For the chemical reaction in the tunnel junctions involving H_2 molecules (switching of the cell atmosphere from air to 2% H_2 in N_2), shown in Fig. S11e-h, the device has almost the same response

regardless of the external illumination: the data in Fig. S11e were obtained without light illumination, the data in Fig. S11f were obtained after illumination with light wavelength larger than 500 nm, the data in Fig. S11g were obtained after illumination with light wavelength in the range of 500-750 nm, and Fig. S11h was measured after illumination with light wavelength larger than 800 nm. It means that the light illumination condition used here (power density of ~0.1 W cm^{-2}) has no effect on the reaction in the tunnel junctions involving H_2 molecules after the reaction in air.

S16. Estimation of temperature rise in the tunnel junctions

Temperature rise in the tunnel junctions under 2.5 V bias was determined using the combination of theoretical calculations and experimental measurements. The temperature at the substrate surface was experimentally measured to be 25 °C above the room temperature (21 °C). The temperature rise in the substrate ΔT_{sub} is related to the heat flux density propagating into the substrate q_{sub} (generated by the tunnelling current) according to the Fourier's law $\nabla T_{sub} = q_{sub}/h$, where h is the thermal conductivity of silica. Assuming the heat dissipation in a symmetric sample holder with half of a total generated heat going into the substrate $q_{sub} = -1/2 \cdot En/S$, where $E = eV$ is the energy released upon relaxation by each of the tunnelled electron (here it is taken into account that radiation is a very minor channel in the electron relaxation), $n = I/e$ is the carrier flux and S is the array area per nanorod (here I is the current through each nanorod and e is the electron charge). Taking experimentally measured values of $I = 180$ pA and $S = 10^{-14} m^2$, one obtains the temperature gradient in the substrate $\nabla T_{sub} = 17.3$ °C/mm. Following the numerical procedure from [37], it was found that there is no additional change of the temperature in the nanorod array towards the area of the tunnelling junctions. Summarizing all temperature changes, the temperature rise in the tunnel junction area under 2.5 V bias was estimated to be 42 °C.

S17. Estimation of energy involved in the chemical reactions

Under a forward bias of 2.5 V (tunnelling current of ~0.09 A), the tunnel current through each nanorod is approximately 180 pA, considering a tunnelling area of ~4 mm^2 and a nanorod areal density of 1.25×10^{10} cm^{-2}. During the reaction period of about 400 s, the total input energy on each nanorod is about 180 nJ. Throughout the oxidation or reduction of tunnel junctions, O_2 or H_2 molecules are dissociated by hot electrons to form surface species, which subsequently oxidize a PLH monolayer or reduce the oxidized PLH monolayer. We can estimate a lower bound for the energy involved in the reactions under the assumption that one hot electron is used for the dissociation of one O_2 or H_2 molecule [13,14,40]. Considering at least one monolayer of surface species covering a nanorod tip of 66 nm in diameter involved in each reaction, approximately 10^5 molecules need to be dissociated, which corresponds to a minimum of 4×10^{-5} nJ energy required for the reaction in one tunnel junction. Thus, about 10^{-5}% of the input electric energy is used for each chemical reaction during the reaction period. This value is limited only by a small number of reactants which are available in the nanoreactor and much more hot electrons are available for reaction if the reactants will be supplied.

S18. Operation of electrically-driven nanorod metamaterial in ethanol

It is also possible to operate electrically-driven plasmonic nanorod metamaterials in liquid environment, which offers increased flexibility with regards of sample handling and preparation for sensing and chemical reaction applications. Because the EGaIn droplet is protected by a native skin of Ga_2O_3, it can keep a stable shape and work well in a liquid environment such as ethanol. This is confirmed by the measured emission spectra shown in Fig. S12. This extends the applications of the proposed approach for chemical reaction stimulation, monitoring and sensing in liquids and a microfluidic environment.
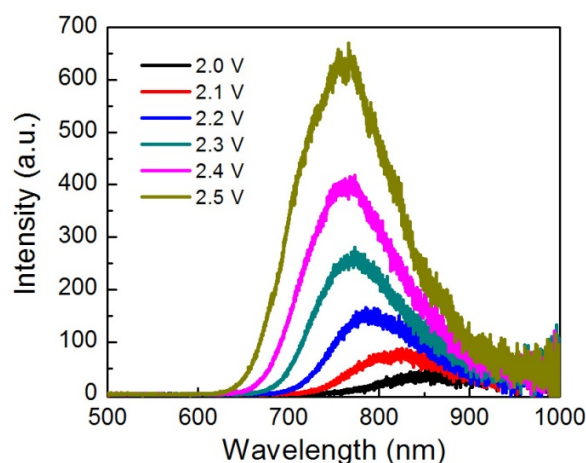
Figure S12 | Operation of electrically-driven metamaterial in ethanol. Measured emission spectra of an electrically-driven plasmonic nanorod metamaterial based on metal-polymer-metal tunnel junctions when operated in ethanol.

References

S1. Evans, P. *et al.* Growth and properties of gold and nickel nanorods in thin film alumina. *Nanotechnology* **17**, 5746–5753 (2006).

S2. Nasir, M. E., Peruch, S., Vasilantonakis, N., Wardley, W. P., Dickson, W., Wurtz, G. A. & Zayats, A. V. Tuning the effective plasma frequency of nanorod metamaterials from visible to telecom wavelengths. *Appl. Phys. Lett.* **107**, 121110 (2015).

S3. Williams, K. R., Gupta, K. & Wasilik, M. Etch rates for micromachining process-part II. *J. Microelectromech. Sys.* **12**, 761–778 (2003).

S4. Dekker A. J. *Solid State Physics* (Prentice-Hall, 1958)

S5. Kittel C. *Introduction to Solid State Physics*, 8th Ed. (Wiley, 2005).

S6. Ando, Y. & Itoh, T. Calculation of transmission tunneling current across arbitrary potential barriers. *J. Appl. Phys.* **61**, 1497–1502 (1987).

S7. Cademartiri, L. *et al.* Electrical resistance of Ag[TS]-S(CH$_2$)$_{n-1}$CH$_3$//Ga$_2$O$_3$/EGaIn tunneling junctions. *J. Phys. Chem. C* **116**, 10848–10860 (2012).

S8. Uskov, A. V., Khurgin, J. B., Protsenko, I. E., Smetanin, I. V. & Bouhelier, A. Excitation of plasmonic nanoantennas by nonresonant and resonant electron tunneling. *Nanoscale* **8**, 14573–14579 (2016).

S9. Belenov, E. M., Luskinovich, P. N., Romanenko, V. I., Sobolev, A. G. & Uskov, A. V. Emission of surface electromagnetic waves in the case of resonance tunneling of electrons. *Sov. J. Quantum Electron.* **17**, 1348–1352 (1987).

S10. Chen, C., Bobisch, C. A. & Ho, W. Visualization of Fermi's golden rule through imaging of light emission from atomic silver chains. *Science* **325**, 981–985 (2009).